

## THE CHANDRA X-RAY OBSERVATORY RESOLVES THE X-RAY MORPHOLOGY AND SPECTRA OF A JET IN PKS 0637–752

G. CHARTAS,<sup>1</sup> D. M. WORRALL,<sup>2,3</sup> M. BIRKINSHAW,<sup>2,3</sup> M. CRESITELLO-DITTMAR,<sup>3</sup> W. CUI,<sup>4</sup> K. K. GHOSH,<sup>5</sup> D. E. HARRIS,<sup>3</sup>  
E. J. HOOPER,<sup>3</sup> D. L. JAUNCEY,<sup>6</sup> D.-W. KIM,<sup>3</sup> J. LOVELL,<sup>6</sup> S. MATHUR,<sup>7</sup> D. A. SCHWARTZ,<sup>3</sup> S. J. TINGAY,<sup>8</sup>  
S. N. VIRANI,<sup>3</sup> AND B. J. WILKES<sup>3</sup>

Received 2000 March 10; accepted 2000 May 11

### ABSTRACT

The core-dominated radio-loud quasar PKS 0637–752 ( $z = 0.654$ ) was the first celestial object observed with the *Chandra X-Ray Observatory*, offering the early surprise of the detection of a remarkable X-ray jet. Several observations with a variety of detector configurations contribute to a total exposure time with the *Chandra* ACIS of about 100 ks. A spatial analysis of all the available X-ray data, making use of *Chandra*'s spatial resolving power of about  $0''.4$ , reveals a jet that extends about  $10''$  to the west of the nucleus. At least four X-ray knots are resolved along the jet, which contains about 5% of the overall X-ray luminosity of the source. Previous observations of PKS 0637–752 in the radio band had identified a kiloparsec-scale radio jet extending to the west of the quasar. The X-ray and radio jets are similar in shape, intensity distribution, and angular structure out to about  $9''$ , after which the X-ray brightness decreases more rapidly and the radio jet turns abruptly to the north. The X-ray luminosity of the total source is  $\log L_x \approx 45.8$  ergs s<sup>-1</sup> (2–10 keV) and appears not to have changed since it was observed with *ASCA* in 1996 November. We present the results of fitting a variety of emission models to the observed spectral distribution, comment on the nonexistence of emission lines recently reported in the *ASCA* observations of PKS 0637–752, and briefly discuss plausible X-ray emission mechanisms.

*Subject headings:* galaxies: active — galaxies: jets — quasars: individual (PKS 0637–752) — X-rays: galaxies

### 1. INTRODUCTION

Until recently, most of our knowledge regarding the spatial structure and spectral shape of extragalactic jets has relied on observations performed in the radio and optical bands. X-ray detections and upper limits have provided insights into the physical conditions responsible for the observed radiation from knots and hot spots in extragalactic radio jets. However, in most cases the poor spectral and spatial resolution available has made the interpretation of the X-ray data difficult. The spectral energy distributions (SEDs) seen from jets have been ascribed to combinations of synchrotron radiation, synchrotron self-Compton (SSC) radiation, and thermal bremsstrahlung from shock-heated gas near the jets. In particular, the synchrotron and SSC models have been successfully employed to explain the X-ray emission from hot spots and jets in M87 (Biretta, Stern, & Harris 1991), Cygnus A (Harris, Carilli, & Perley 1994), and 3C 295 (Harris et al. 2000). In the cases of 3C 273 (Harris & Stern 1987) and Pictor A (Meisenheimer et al. 1989), none of the standard processes yield satisfactory results.

The *Chandra X-Ray Observatory*, launched on 1999 July 23, provides a significant improvement over previous missions in combined spatial and spectral resolution (see Weisskopf & O'Dell 1997; van Speybroeck et al. 1997), which we expect will result in a significant increase in the number of detected and resolved X-ray jets. PKS 0637–752 is the first X-ray jet to have been discovered by *Chandra*. The quasar was originally detected in X-rays with the *Einstein Observatory* (Elvis & Fabbiano 1984). Since then a peculiar emission-line feature at  $\sim 0.97$  keV was claimed in an *ASCA* SIS observation of the source (Yaqoob et al. 1998). One of two *Ginga* observations of PKS 0637–752 has been reported as showing a marginal detection of an Fe  $K\alpha$  line with an equivalent width of  $103 \pm 85$  eV ( $\pm 1 \sigma$  errors; Lawson & Turner 1997).

In § 2 we describe the spectral and spatial analysis of the core and jet and our observations of the radio jet. The properties of sources in the vicinity of PKS 0637–752 are also briefly presented. Section 3 contains a brief description of our attempt to apply standard jet models to the observed SED of PKS 0637–752. We provide a thorough investigation of the underlying emission processes in a companion paper (Schwartz et al. 2000), where more complex models are considered.

In the following, we assume a Friedman cosmology with  $H_0 = 50$  km s<sup>-1</sup> Mpc<sup>-1</sup> and  $q_0 = 0$ .

### 2. DATA REDUCTION AND ANALYSIS

Twenty-five observations of PKS 0637–752 were made between 1999 August 14 and August 24 with the *Chandra* ACIS-S during the orbital activation and checkout phase of the mission. Table 1 summarizes several ACIS configuration parameters, 50% encircled energy radii, exposure times, and estimated net count rates over the entire ACIS band corresponding to each individual observation.

<sup>1</sup> Astronomy and Astrophysics Department, Pennsylvania State University, University Park, PA 16802; chartas@astro.psu.edu.

<sup>2</sup> Department of Physics, University of Bristol, England.

<sup>3</sup> Harvard-Smithsonian Center For Astrophysics, Cambridge, MA 02138.

<sup>4</sup> MIT Center for Space Research, 70 Vassar Street, Cambridge, MA 02139.

<sup>5</sup> Space Sciences Laboratory, NASA/Marshall Space Flight Center, Mail Code ES84, Huntsville, AL 35812.

<sup>6</sup> Australia Telescope National Facility, P.O. Box 76, Epping, NSW 2121, Australia.

<sup>7</sup> Ohio State University.

<sup>8</sup> Jet Propulsion Laboratory, California Institute of Technology, Mail Stop 238-332, 4800 Oak Grove Drive, Pasadena, CA 91109.

TABLE 1  
*C*<sub>HANDRA</sub> OBSERVATIONS OF PKS 0637–752

Observation Date (1)	Observation ID (2)	Exposure (s) (3)	Frame Time (s) (4)	SIM <sub>x</sub> (mm) (5)	Src <sub>y</sub> (arcmin) (6)	Src <sub>x</sub> (arcmin) (7)	HPR (arcsec) (8)	<i>N</i> <sub>Core</sub> (counts) (9)	<i>N</i> <sub>In</sub> (counts) (10)	<i>N</i> <sub>Out</sub> (counts) (11)	<i>N</i> <sub>Bg</sub> (counts arcsec <sup>-2</sup> ) (12)
1999-08-14T10:49:39	1051	1034	3.24	0.0	2.0	1.0	1.05	408	5	28	0.028
1999-08-14T11:36:00	1052	1041	3.24	0.0	2.0	1.0	0.95	391	2	28	0.045
1999-08-14T13:53:09	62558	19116	3.24	1.0	0.0	0.0	1.00	7196	63	502	0.498
1999-08-14T19:15:24	62556	5068	3.24	0.9	0.0	0.0	0.95	1799	18	119	0.111
1999-08-14T20:51:39	62555	5138	3.24	0.65	0.0	0.0	0.80	1554	18	155	0.108
1999-08-14T22:24:18	62554	11367	3.24	0.25	0.0	0.0	0.55	2664	40	281	0.267
1999-08-15T02:49:29	62553	5232	1.541	0.0	0.0	0.0	0.40	2098	16	188	0.110
1999-08-15T04:18:30	62552	5213	1.541	-0.5	0.0	0.0	0.70	2373	20	148	0.100
1999-08-15T05:55:56	62551	5343	1.541	-0.25	0.0	0.0	0.40	2108	18	148	0.108
1999-08-15T07:36:04	62550	5469	1.541	0.2	0.0	0.0	0.50	2266	33	128	0.099
1999-08-15T09:12:04	62549	6426	1.541	0.5	0.0	0.0	0.55	2777	22	152	0.133
1999-08-16T06:05:37	1055	2036	3.24	0.0	0.0	0.0	0.85	659	8	50	0.057
1999-08-16T06:56:36	1056	1757	3.24	0.0	1.4	1.4	1.10	744	5	42	0.061
1999-08-16T17:43:28	1058	1757	3.24	0.0	-1.4	1.4	1.00	710	7	41	0.044
1999-08-16T18:29:48	1059	1760	3.24	0.0	-3.0	-2.8	1.00	555	5	22	0.250
1999-08-16T19:16:07	1060	1760	3.24	0.0	-1.4	-1.4	1.20	781	6	51	0.155
1999-08-16T20:53:19	1062	1760	3.24	0.0	1.4	1.4	1.10	758	9	54	0.097
1999-08-16T21:35:07	1063	1760	3.24	0.0	2.8	-2.8	2.00	1019	15	40	0.115
1999-08-20T02:26:38	472	5809	0.941	1.0	0.0	0.0	1.05	3417	20	140	0.095
1999-08-20T04:54:34	473	4678	0.941	0.11	0.0	0.0	0.4	2206	21	117	0.085
1999-08-20T06:17:37	474	4856	0.941	-0.09	0.0	0.0	0.4	2255	21	112	0.088
1999-08-20T07:54:18	475	4856	3.24	-0.19	0.0	0.0	0.45	2386	22	100	0.088
1999-08-20T09:30:57	476	4856	0.941	-0.98	0.0	0.0	1.10	2967	10	113	0.167

NOTES.—Col. (5): SIM<sub>x</sub> is the distance along the optical axis of the scientific instrument module from the best focus location; col. (6): Src<sub>y</sub> is the distance along the y-direction from the nominal aim point; *y* is the direction of grating dispersion; the ACIS-S array nominal aim point falls on chip S3, 2.0 to the right (+*y*) of the edge of the chip; col. (7): Src<sub>x</sub> is the distance along the *z*-direction from the nominal aim point; *z* is the direction normal to the grating dispersion; col. (8): HPR is the half-power radius; col. (9): *N*<sub>Core</sub> are the detected events from the core component extracted from circles centered on the core with radii of 5"; col. (10): *N*<sub>In</sub> are the detected events from the inner jet component extracted from rectangular regions having the left lower corners set at (*x*<sub>c</sub> + 4", *y*<sub>c</sub> - 1"5) and the right upper corners set at (*x*<sub>c</sub> + 6"5, *y*<sub>c</sub> + 1"5), where *x*<sub>c</sub>, *y*<sub>c</sub> are the centroid locations of the core for each observation; col. (11): *N*<sub>Out</sub> are the detected events from the outer jet component extracted from circles centered on the X-ray knot WK 8.9 with radii of 2"5; col. (12): *N*<sub>Bg</sub> are the detected background events arcsec<sup>-2</sup> extracted from annuli centered on the core with inner and outer radii of 45" and 55", respectively. Only events with standard ASCA grades 0, 2, 3, 4, and 6 were extracted.

The primary purpose of these observations was to focus the ACIS-S detector (in SIM<sub>x</sub>) and to determine the position of the *Chandra* mirror optical axis by pointing to PKS 0637–752 at different (Src<sub>y</sub>, Src<sub>z</sub>) offsets. (Definitions for Src<sub>y</sub>, Src<sub>z</sub>, and SIM<sub>x</sub> are presented in the notes of Table 1.)

The spectral and spatial analysis of the data is complicated by the numerous configurations used during the observation of PKS 0637–752. The point-spread function (PSF) corresponding to each observation differs significantly because of the nature of the calibration being performed. In particular, the 50% encircled energy radii varied between 0".4 at best focus and about 1" at 3' off-axis pointing or poor focus (see Fig. 1 and Table 1). The jet (§ 2.1) was spatially resolved from the core and made little impact on the determination of the best focus and best optical axis location.

A second important property of the data that we have accounted for in our analysis is pileup (see § 6.17 of the *Chandra Observatory Guide*).<sup>9</sup> Whenever the separation of two or more X-ray photons incident on a CCD is less than a few CCD pixels, and their arrival time lies within the same CCD frame readout, the CCD electronics may regard them as a single event with an amplitude given by the sum of the electron charge in the 3 × 3 neighborhood of the pixel with the maximum detected charge. A detected CCD event is characterized by the total charge within the 3 × 3 island and the distribution of the charge (often referred to as the grade of the event) within that island. Pileup may alter the grades and charges of events, thus affecting both their spatial and spectral distribution. A manifestation of pileup in observed spectra may be a reduction of detected events, spectral hardening of the continuum component, and the apparent distortion of the PSF of pointlike objects.

The presence of pileup is apparent in the observed spectra of the core of PKS 0637–752. In particular, we observed a significant change in count rate of the core component of PKS 0637–752 as a function of focus position (SIM<sub>x</sub>) along the optical axis. As shown in Figure 1, the apparent

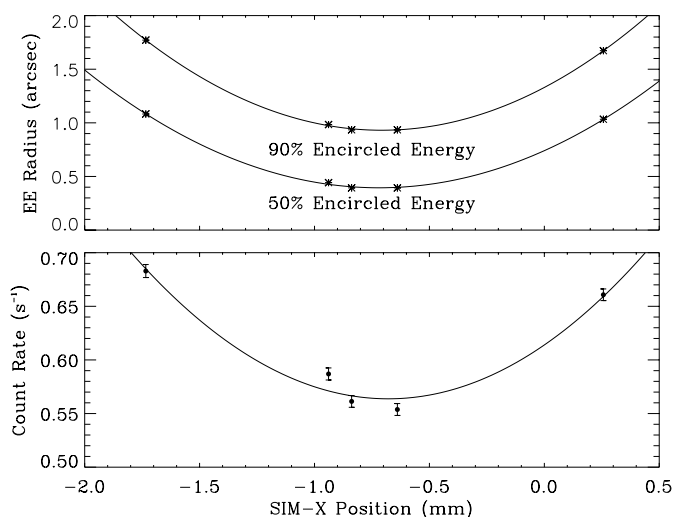


FIG. 1.—50% and 90% encircled energy and observed count rate as a function of SIM<sub>x</sub> position. The increased PSF half-power radius (*upper panel*) and count rate (*lower panel*) with SIM position away from best focus increases because pileup decreases.

count rate is lowest at the best focus position and increases as the scientific instrument module (SIM) is moved away from this location. A parabolic function was used to fit the count rates and encircled energy radii as a function of focus position. We estimate a SIM<sub>x</sub> focus location of  $\sim -0.7$  mm corresponding to the minimum of both count rate and encircled energy radii.

Count rates for a similar test performed with a shorter CCD frame readout time showed a similar behavior but with detected count rates systematically larger than those for the standard 3.24 s full-frame readout time. The observed count rate variation is due to the pileup effect and not intrinsic to the quasar. As the telescope approaches best focus, most photons fall onto a single CCD pixel, and the enhanced pileup leads to a decrease in detected count rate.

Correcting a CCD observation of an X-ray source for pileup is quite complicated. The dependence of pileup on several effects such as the incident X-ray flux, the spectral and spatial distribution of the events, the grade selection scheme used, and the detection cell size adopted make the problem of restoring to the unpiled up spectrum nontrivial.

Fortunately, the jet of PKS 0637–752 is not affected by pileup since the jet is a relatively low count rate extended source.

## 2.1. X-Ray Morphology

To obtain a high signal-to-noise image of PKS 0637–752, we made use of all observations with observed half-power radius (HPR) less than 1".2. For each observation, a PSF appropriate for the focus and aim point position was created employing the simulation tool MARX v2.2 (Wise et al. 1997).<sup>10</sup> The input spectrum assumed in the PSF simulations was that derived from the best-fit *Chandra* spectrum of the outer jet of PKS 0637–752 (see § 2.3). Specifically, we used an absorbed power law with a column density of  $N_{\text{H}} = 11.8 \times 10^{20} \text{ cm}^{-2}$  and a photon index of 1.83. We examined the sensitivity of the resulting deconvolved image to the spectral slope used in the PSF simulations and found no particular spectral dependence for photon indices ranging between 1.7 and 2.3.

The simulated PSFs were binned to a subpixel scale of 0".125. To avoid aliasing effects, the *Chandra* X-Ray Center (CXC) processing incorporates a randomization of each position by  $\pm 0".246$  (1 ACIS pixel = 0".492). Residual errors in the aspect solution are expected to add a “blurring” to detected photon positions of  $\sim 0".3$  rms in diameter. To simulate aspect errors and position randomization, we convolved each generated PSF with a Gaussian with  $\sigma = 0".25$ . The X-ray photon event positions for each observation were also binned to 0".125, and the resulting X-ray image is shown in Figure 2 (*top panel*). A maximum likelihood deconvolution technique, using the appropriate simulated PSF, was applied to each individual observation. The resulting deconvolved images were aligned on the core centroid and combined to produce the total deconvolved image of PKS 0637–752 shown in Figure 2 (*middle panel*). The effective resolution of the deconvolved X-ray image was estimated by deconvolving the simulated PSFs of each observation, stacking the simulated PSFs, and determining the FWHM of the deconvolved stacked PSF. Our analysis yields an effective resolution for the stacked deconvolved image of  $\sim 0".37$ . The PSFs simulated for this analysis are

<sup>9</sup> <http://asc.harvard.edu/udocs/docs/POG/MOPG/index.html>.

<sup>10</sup> <http://space.mit.edu/ASC/MARX/>.

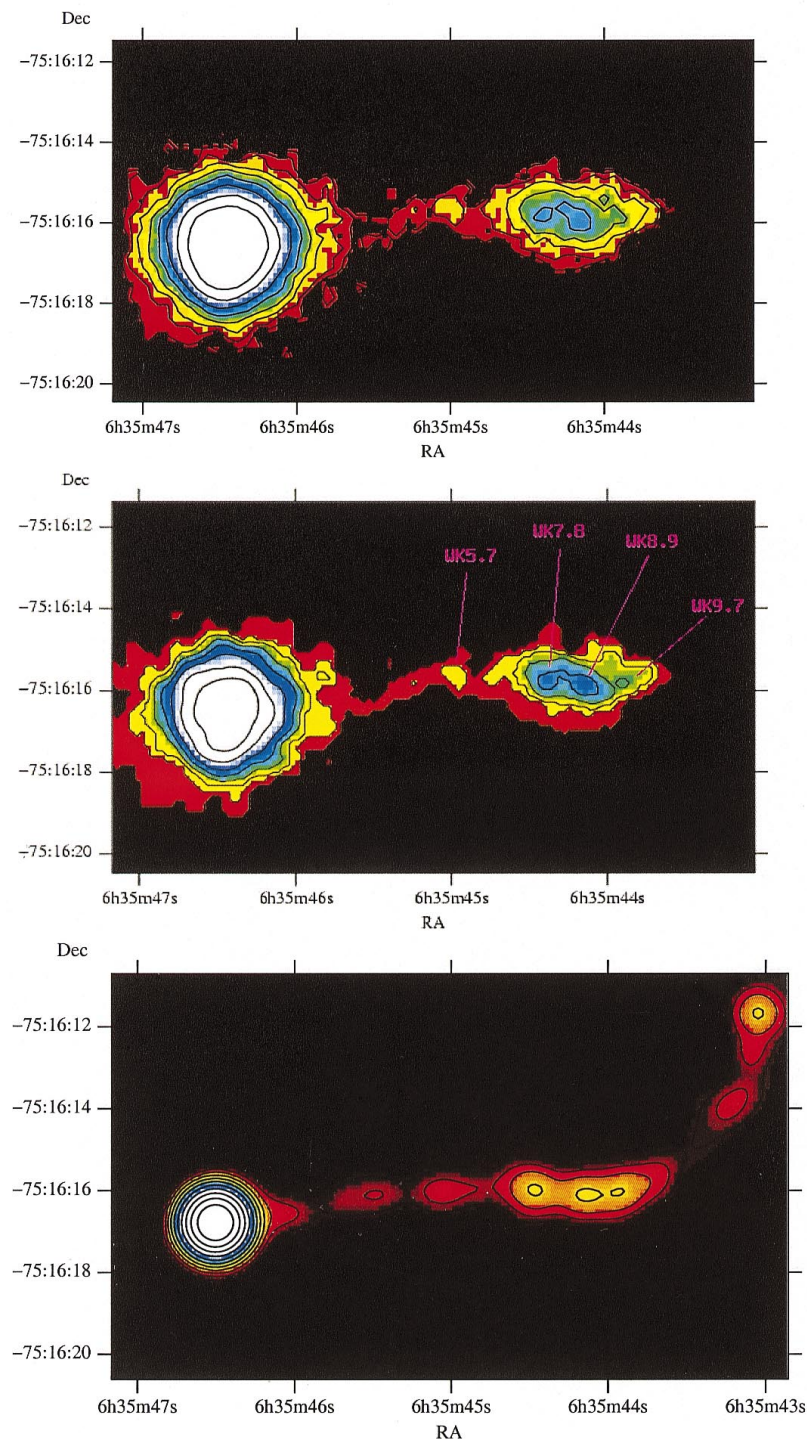


FIG. 2.—*Top panel*: X-ray image of PKS 0637–752 created by stacking all observations with half-power radii less than  $1''.2$ . *Middle panel*: Total maximum likelihood deconvolved X-ray image of PKS 0637–752 produced by stacking all deconvolved images of observations with half-power radii less than  $1''.2$ . *Lower panel*: ATCA 8.6 GHz image of PKS 0637–752 restored with a circular beam of  $0''.84$  FWHM.

not appropriate for the piled up region of the core. This is why any deconvolved structure within  $\sim 2''$  from the core should not be considered real. The jet region beyond  $\sim 2''$  does not suffer from pileup effects, and the simulated PSFs are appropriate for deconvolving the jet region. Several interesting structures have become more apparent in Figure 2 (*middle panel*). A well-collimated X-ray jet is seen to originate in the core and to extend approximately  $10''$  to the west, and within the jet at least four knots are clearly resolved.

## 2.2. Radio Morphology

The radio jet was imaged at 4.8 and 8.6 GHz on 1999 August 19 and on 1999 September 21 using the Australia Telescope Compact Array (ATCA), which has a similar arc-second resolution at 8.6 GHz as *Chandra* and so provides a powerful structural comparison. The resulting 8.6 GHz radio image (Schwartz et al. 2000; Lovell et al. 2000) is shown in Figure 2 (*lower panel*), where the coincidence with the X-ray knots is apparent. The three farthest X-ray knots,

WK7.8, WK8.9, and WK9.7, appear to be embedded in extended and diffuse X-ray emission. The X-ray jet appears to bend southwest after its encounter with the first X-ray knot, WK5.7, and then bend northwest after the encounter with the fourth X-ray knot WK9.7. The radio image of the PKS 0637–752 jet (Fig. 2, lower panel) indicates that the radio jet also bends in the northwest direction after its encounter with WK9.7. The X-ray emission after knot WK9.7 drops substantially to become undetectable after several arcseconds. A comparison between the X-ray and radio intensity profile along the jet (Fig. 3) shows close alignment of the X-ray and radio jets out to 10" and relatively well-matched X-ray and radio knots at 5".7, 7".8, 8".9, and 9".7 from the core. The radio profile in Figure 3 was produced from the 8.6 GHz image (Schwartz et al. 2000; Lovell et al. 2000). The position angles of the radio and X-ray jets appear to be similar, as shown in Figure 4, where we have used the deconvolved X-ray image and the same 8.6 GHz radio map as before to plot the position angle of the ridges of peak radio and X-ray brightness along the jet with respect to the core of PKS 0637–752.

### 2.3. Spectral Analysis of the Core Component

To determine the continuum spectral shape of the core component of PKS 0637–752, we considered only the two least piled up on-axis observations corresponding to observations 472 and 476. The expected percent loss of counts due to pileup, based on our simulations, is  $\sim 12\%$ . X-ray events were extracted within a circle centered on the core of PKS 0637–752 with a radius of 5", and events with standard *ASCA* grades 0, 2, 3, 4, and 6 only were selected. The background was determined by extracting events within annuli centered on the core with inner and outer radii of 15" and 20", respectively. Spectra were binned to have a minimum of 20 counts per bin such that  $\chi^2$  statistics can be used without low count corrections.

Spectral fits were performed using the standard software tool XSPEC (Arnaud 1996), and we compared these results

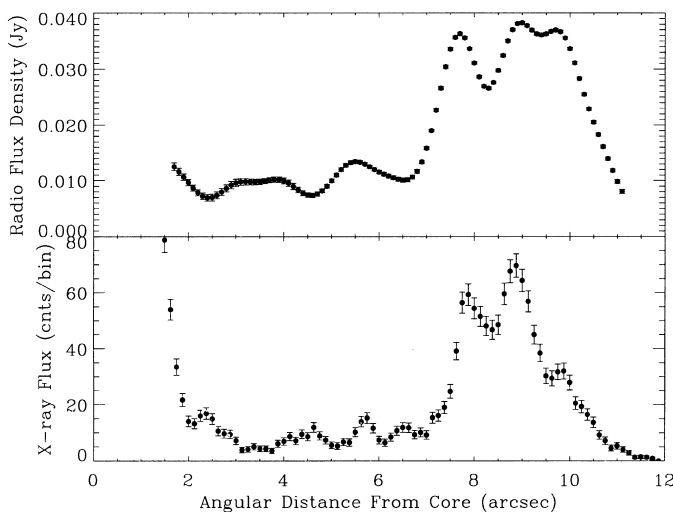


FIG. 3.—X-ray and radio intensity profile of jet along right ascension direction integrated  $\pm 1''$  perpendicular to the jet. The X-ray profile provides counts in 0".125 increments, and the radio profile provides the 8.6 GHz flux density beam $^{-1}$  in 0".1 bins. The X-ray profile was produced from the deconvolved X-ray image, and the radio profile was produced from the 8.6 GHz image (Schwartz et al. 2000; Lovell et al. 2000). The 8.6 GHz beam width is  $\sim 1''$  FWHM, and the effective resolution (FWHM) of the X-ray image after deconvolution is  $\sim 0.4''$ .

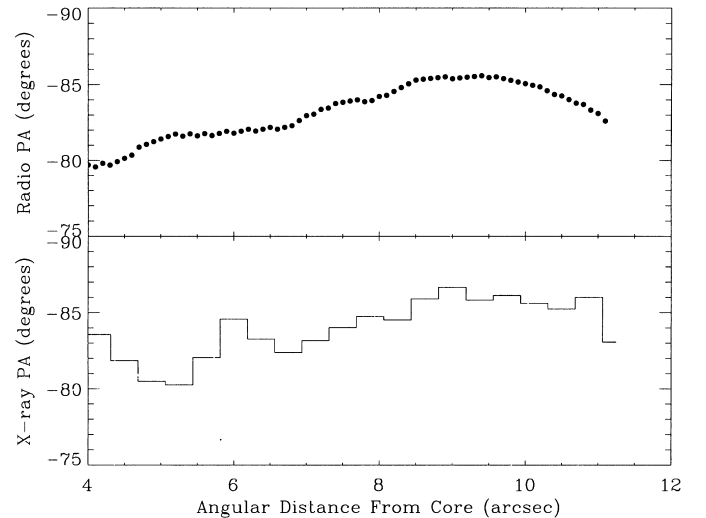


FIG. 4.—X-ray and radio position angle of the ridge of peak brightness along the jet with respect to the core of PKS 0637–752. The radio position angle plot was derived from the 8.6 GHz image (Schwartz et al. 2000; Lovell et al. 2000).

to those provided by the simulator-based spectral fitting tool LYNX (Chartas et al. 2000, in preparation). A brief description of the LYNX fitting tool is provided in the Appendix. The telescope pointings are intentionally dithered for the observations of PKS 0637–752 in a Lissajous pattern with an amplitude of about 16" such that small-scale nonuniformities in the CCD quantum efficiency are averaged out. The selected aim point of the telescope for most of the PKS 0637–752 observations was set within 10" from the boundary between amplifier nodes 0 and 1 of the S3 CCD of ACIS, resulting in the source being dithered across the two nodes. To account for the difference in amplifier gains between nodes 0 and 1, events detected from the core component of PKS 0637–752 were separated into two spectra containing events detected from a single node, either 0 or 1. For fitting the spectra with XSPEC, we used the appropriate response and ancillary files provided by the CXC. All errors on best-fit spectral parameters quoted in this paper are at the 90% confidence level unless mentioned otherwise.

Specifically, we used the *Chandra* Interactive Analysis of Observations (CIAO) v1.1 tools MKRMF and MKARF to generate response and ancillary files. The focal plane temperature was  $-100^\circ\text{C}$  for these observations. The exposure times of each observation are listed in Table 1. A simple power-law plus cold, neutral absorber model was used to fit the core spectrum of PKS 0637–752. The best-fit parameters of the spectral fits are shown in Table 2.

Fit 2 of Table 2 was performed in the energy range 0.2–6.0 keV. The reduced  $\chi^2_\nu$  of 1.1 for 235 degrees of freedom is acceptable in a statistical sense. However, the best-fit value of  $(3.5 \pm 0.5) \times 10^{20} \text{ cm}^{-2}$  for the column density is significantly below the previously observed *ASCA* value of  $(9 \pm 3) \times 10^{20} \text{ cm}^{-2}$  and the Galactic column density of  $9.1 \times 10^{20} \text{ cm}^{-2}$  (Dickey & Lockman 1990). In fit 3 of Table 2, we fixed the neutral column density to the Galactic value and obtained a reduced  $\chi^2_\nu$  of 1.7 for 236 degrees of freedom.

We searched for systematic errors in the spectral fits of the core by repeating fit 3 of Table 2 allowing for the lower bound of the fitted energy range to vary between 0.2 and 1.5

TABLE 2

MODEL PARAMETERS DETERMINED FROM SPECTRAL FITS TO THE *CHANDRA* ACIS-S SPECTRA OF THE CORE COMPONENT OF PKS 0637–752

Fit <sup>a</sup>	Range (keV)	$\Gamma$	$N_{\text{H}}$ ( $z = 0$ ) ( $10^{20} \text{ cm}^{-2}$ )	Flux <sup>b</sup> ( $10^{-12} \text{ ergs s}^{-1} \text{ cm}^{-2}$ )	Flux Density at 1 keV ( $10^{-13} \text{ ergs s}^{-1} \text{ cm}^{-2} \text{ keV}^{-1}$ )	$L_{\text{x}}^{\text{c}}$ ( $10^{45} \text{ ergs s}^{-1}$ )	$\chi^2_{\nu}/(\text{dof})$
1.....	0.2–6.0	$1.77^{+0.1}_{-0.1}$	$11^{+2.0}_{-2.0}$	1.1 (2.2)	7.4	5.9 (6.4)	1.4 (86)
2.....	0.2–6.0	$1.69^{+0.05}_{-0.05}$	$3.5^{+0.5}_{-0.5}$	1.3 (2.2)	7.8	4.8 (6.0)	1.1 (235)
3.....	0.2–6.0	$2.00^{+0.04}_{-0.04}$	9.0 (fixed)	1.3 (1.7)	8.5	7.8 (5.5)	1.7 (236)
4.....	1.0–6.0	$1.76^{+0.08}_{-0.08}$	9.0 (fixed)	1.1 (2.2)	7.5	5.6 (6.1)	1.1 (128)

<sup>a</sup> All fits incorporate a power-law spectrum plus absorption due to cold material at solar abundances. Spectral fit 1 was performed with the LYNX spectral fitting tool with events extracted from node 1 only. Spectral fits 2, 3, and 4 were performed with the XSPEC tool with events extracted from nodes 0 and 1.

<sup>b</sup> Fluxes calculated in the ranges 0.2–2 keV and 2–10 keV (quoted in parentheses). X-ray fluxes are not corrected for Galactic absorption.

<sup>c</sup> Luminosities calculated in the ranges 0.2–2 keV and 2–10 keV (quoted in parentheses). Luminosities are in the rest frame and are corrected for Galactic absorption.

keV. We find that the best-fit XSPEC value for the spectral slope varies between  $2.00 \pm 0.04$  and  $1.8 \pm 0.05$  for the lower bounds of the fit ranging between 0.2 and 0.8 keV, respectively, and remains constant at about 1.8 for the lower bounds of the fit ranging between 0.8 and 1.5 keV. Plausible explanations for the variation of the spectral slope with the lower bound of the fit include pileup effects of the spectrum of the core and/or uncertainties in the available response and ancillary files at energies below  $\sim 0.5$  keV. We therefore restricted the XSPEC fits of the core component to energies above 1 keV with the neutral column density parameter held fixed at the Galactic value of  $N_{\text{H}} = 9 \times 10^{20} \text{ cm}^{-2}$ . The fit within the 1–6 keV range yields a photon index of  $1.76 \pm 0.1$  (fit 4 in Table 2).

Best-fit parameters to the core component were also obtained utilizing the simulator based tool, LYNX (fit 1 in Table 2), and restricting the energy range of the fit between 0.2 and 6.0 keV. This fit yields a column density of  $(11 \pm 2) \times 10^{20} \text{ cm}^{-2}$  that is consistent with the Galactic

value and a photon index of  $1.77 \pm 0.1$  that is consistent with *Ginga* and *ASCA* results (Lawson et al. 1992; Lawson & Turner 1997; Yaqoob et al. 1998). All X-ray photon indices,  $\Gamma$ , and energy indices,  $\alpha_E$ , follow the convention of flux density  $\propto \nu^{-(\Gamma-1)}$ , where flux density is in units of  $\text{ergs cm}^{-2} \text{ s}^{-1} \text{ Hz}^{-1}$  and  $\Gamma = \alpha_E + 1$ .

The difference between the LYNX and XSPEC fit results for the spectrum of the core of PKS 0637–752 can be partially attributed to the presence of pileup in the spectrum of the core, which is not modeled in the XSPEC fits.

In Figure 5, we present the spectrum of the core component of PKS 0637–752 corresponding to observation 476, together with the best-fit model (fit 1 from Table 2) and the ratio of observed spectrum to model. The estimated 2–10 keV flux of  $2.2 \times 10^{-12} \text{ ergs s}^{-1} \text{ cm}^{-2}$  (from fit 1 of Table 2) indicates that the core flux has not varied, within the quoted error bars, since the 1996 November *ASCA* observations, especially when one considers that the *ASCA* observed flux corresponds to all emission within a 3' radius

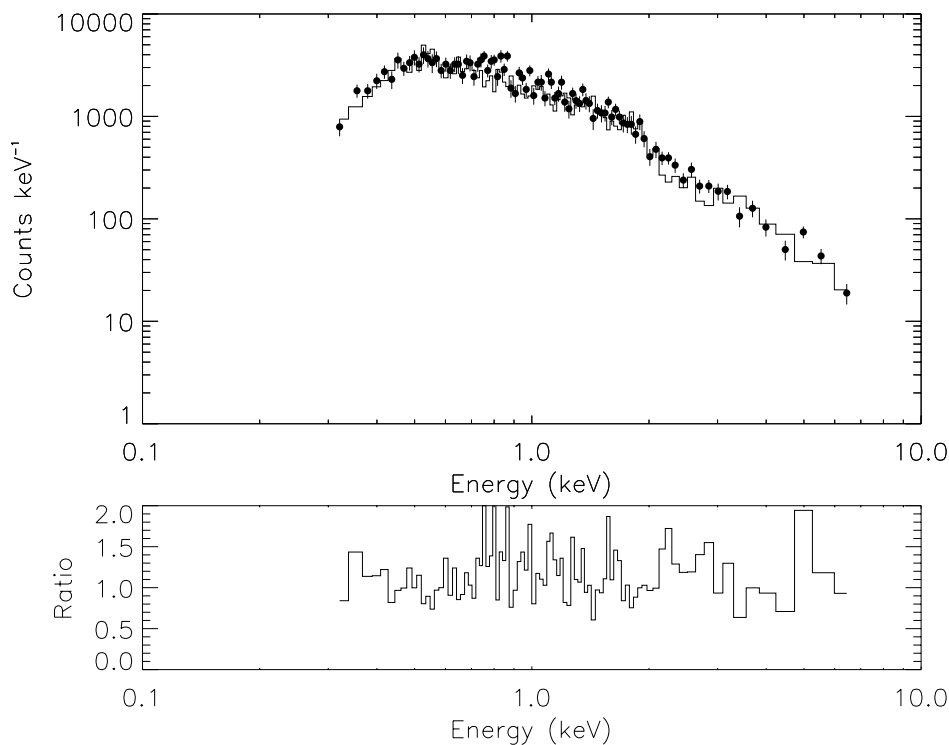


FIG. 5.—Spectrum from observation 476 of core component of PKS 0637–752 with best-fit model (fit 1 from Table 2)

of the core. X-ray fluxes quoted in this paper are not corrected for Galactic absorption.

We chose to improve the signal-to-noise ratio for the detection of faint emission lines in the spectrum of PKS 0637–752 by stacking all the available spectra. In the summed spectrum, we expect that pileup will distort the continuum shape and cause emission lines to appear with overtone “ghosts” at higher energies. We initially produced a model that best fit the continuum component of the stacked spectrum. The region in the vicinity of the mirror Ir edges (see Table 3) was excluded from the fit. In Figure 6, we plot the stacked spectrum of the core component of PKS 0637–752 with the best-fit continuum component. We also show the ratio of the observed-to-best-fit continuum model. The best-fit model yields a reduced  $\chi^2_\nu$  of 0.99 for 147 degrees of freedom (dof). This ratio suggests that no significant emission-line features are present. In particular, we do not detect an emission line in the vicinity of 1 keV and at an equivalent width (EW)  $\sim 60$  eV as suggested by a recent *ASCA* observation of PKS 0637–752 (Yaqoob et al. 1998). An upper limit of 15 eV on EW, at the 90% confidence level, can be placed on any line with energies 0.8–1.2 keV (observed frame) and width of 0–0.2 keV.

There are several spectral features in observed ACIS spectra that do not originate from astrophysical sources but are produced from various sites within the *Chandra*/ACIS instrument. In Table 3, we list all known instrumental spectral features and their origins. The significant instrumental features are the Al-L, C-K, N-K, O-K, and Al-K UV/optical blocking filter absorption edges; the N-K, O-K, and Si-K CCD absorption edges; and the Ir-M high-resolution mirror assembly (HRMA) absorption edges. In the spectra of the core of PKS 0637–752 (see Figs. 5 and 6), the main instrumental spectral features that can be seen are the Ir-M

HRMA absorption edge at 2.085 keV and the O-K $\alpha$  ACIS absorption edge at 0.536 keV.

#### 2.4. Spectral Analysis of the Inner Jet Component

For the purposes of this spectral analysis, we have extracted the spectrum of the jet in a region 4”–6”5 away from the core and define this as the inner jet region. Pileup effects are negligible for the inner jet component because of the extended nature of the emission combined with the relatively low count rate of  $\sim 4 \times 10^{-3}$  counts  $s^{-1}$ . The X-ray image of PKS 0637–752 shown in Figure 2 indicates a degree of curvature in the jet that appears to follow the spatial morphology observed in the radio (Schwartz et al. 2000; Lovell et al. 2000). The X-ray spectrum of the inner jet component was produced by extracting events from all the observations listed in Table 1. The spatial extraction filter chosen was a rectangle with the left lower corner set at  $(x_c + 4'', y_c - 1''.5)$  and the right upper corner set at  $(x_c + 6''.5, y_c + 1''.5)$ , where  $x_c, y_c$  are the centroid locations of the core for each observation. In Figure 7, we show the observed spectrum of the inner jet component with the best-fit model assuming a power-law emission process (fit 3 in Table 4).

Because of the present uncertainties with response matrices below 0.5 keV for the S3 CCD, the spectral fits utilizing XSPEC were performed in the 0.6–4 keV range, and fits utilizing the tool LYNX (which appears to be more reliable at energies below 1 keV) were performed in the 0.2–4 keV range. Model 1 incorporates a simple absorbed power-law model and yields a photon index of  $\Gamma = 2.0 \pm 0.2$  (LYNX; fit 1 in Table 4) or  $\Gamma = 2.27 \pm 0.3$  (XSPEC; fit 3 in Table 4). Model 2 incorporates a Raymond-Smith thermal plasma model and a best-fit column density consistent with the Galactic value and

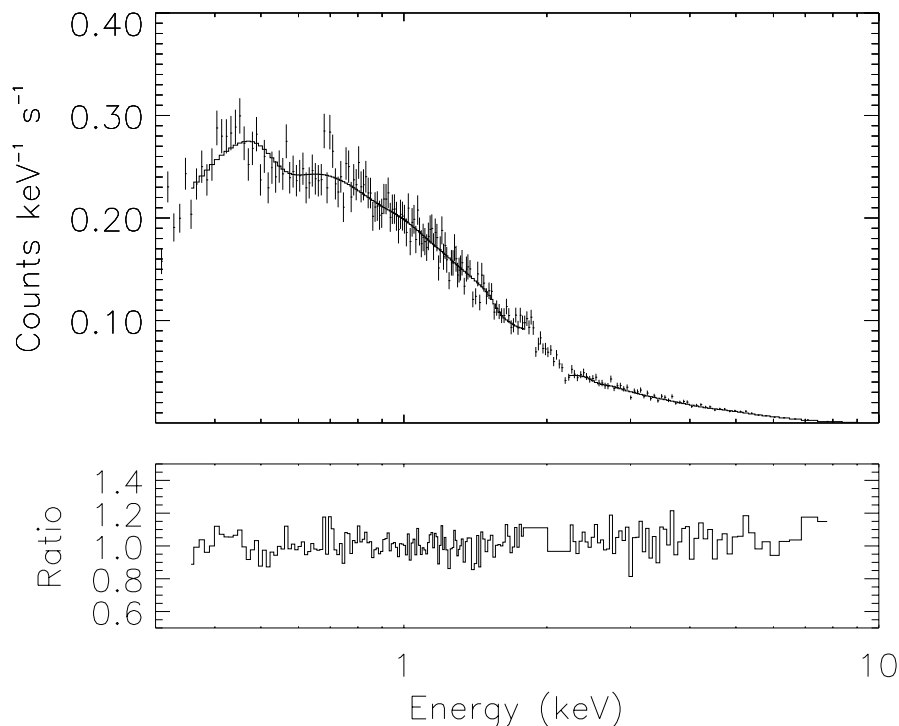


FIG. 6.—Stacked spectrum of the core component of PKS 0637–752. No prominent emission line is detected near 1 keV as claimed in a recent *ASCA* observation of PKS 0637–752.



TABLE 3  
*CHANDRA* ACIS INSTRUMENTAL SPECTRAL FEATURES

Energy (keV)	Spectral Feature <sup>a</sup>	Origin
0.076	Al-L absorption edge	ACIS-OBF
0.105	Si L <sub>3</sub> absorption edge	ACIS-CCD
0.107	Si L <sub>2</sub> absorption edge	ACIS-CCD
0.158	Si L <sub>1</sub> absorption edge	ACIS-CCD
0.285	C K $\alpha$ absorption edge	ACIS-OBF
0.402	N K $\alpha$ absorption edge	ACIS-OBF, ACIS-CCD
0.535	O K $\alpha$ absorption edge	ACIS-OBF, ACIS-CCD
1.486	Al K $\alpha$ fluorescence line	ACIS-CCD
1.559	Al K $\alpha$ absorption edge	ACIS-OBF
1.739	Si K fluorescence line	ACIS-CCD
$E_0 - E_f$ <sup>b</sup>	Si K escape peak	ACIS-CCD
1.841	Si K absorption edge of polysilicon	ACIS-CCD
1.8473	Si K absorption edge of SiO <sub>2</sub>	ACIS-CCD
1.8447	Si K absorption edge of Si <sub>3</sub> N <sub>4</sub>	ACIS-CCD
2.085 <sup>c</sup>	Ir M-V edge	HRMA
2.112	Au M $\alpha_{1,2}$ fluorescence line	ACIS-CCD
2.156 <sup>c</sup>	Ir M-IV edge	HRMA
2.20	Au M $\beta$ fluorescence line	ACIS-CCD
2.410	Au M $\gamma$ fluorescence line	ACIS-CCD
2.549 <sup>c</sup>	Ir M-III edge	HRMA
2.906 <sup>c</sup>	Ir M-II edge	HRMA
3.183 <sup>c</sup>	Ir M-I edge	HRMA
7.469	Ni K $\alpha$ fluorescence line	ACIS-CCD
9.71	Au L $\alpha_1$ fluorescence line	ACIS-CCD
11.44	Au L $\beta_1$ fluorescence line	ACIS-CCD
11.52	Au L $\beta_2$ fluorescence line	ACIS-CCD
15.2- $E_{\text{bias}}$ <sup>d</sup>	4096 ADU—bias level	ACIS-CCD
15.2	4096 ADU	

<sup>a</sup> Additional instrumental spectral features arise due to X-ray absorption fine structure produced in the CCDs and UV/optical blocking filter. These features extend for about a few hundred eV above each of absorption edges of Al-L, C-K, N-K, O-K, Al-K.

<sup>b</sup>  $E_0$  is the energy of the incident photon and  $E_f = 1.739$  is the energy of the silicon fluorescence photons.

<sup>c</sup> Mirror absorption energies from Graessle et al. 1993.

<sup>d</sup> These energies are dependent on the gain and bias levels and will vary from chip to chip.

yields a best-fit temperature of  $2.7 \pm 0.2$  keV (LYNX; fit 2 in Table 4) or  $2.29^{+1.0}_{-0.5}$  keV (XSPEC; fit 4 in Table 4). Abundances were fixed at 0.3 of the cosmic value.

An  $F$ -test between fits 1 and 2 indicates that neither model is significantly preferred over the other. The 2–10 keV X-ray luminosity of the inner jet region, assuming an absorbed power-law model (model 1 in Table 4), is  $0.27 \times 10^{44}$  ergs s<sup>-1</sup>.

### 2.5. Spectral Analysis of the Outer Jet Component

The X-ray spectra for the outer jet component were extracted from circles centered on knot WK8.9 with radii of 2'.5. Only standard *ASCA* grades 0, 2, 3, 4, and 6 were included, and the background was determined by extracting events within annuli centered on the core with inner and outer radii of 15" and 25", respectively. Pileup effects are

TABLE 4  
 MODEL PARAMETERS DETERMINED FROM SPECTRAL FITS TO THE *CHANDRA* ACIS-S SPECTRA OF THE INNER JET COMPONENT OF PKS 0637–752

Model <sup>a</sup>	$\Gamma$ or $T_e$	$T_e$ (keV)	$N_H$ ( $z = 0$ ) ( $10^{20}$ cm <sup>-2</sup> )	Flux <sup>b</sup> ( $10^{-15}$ ergs s <sup>-1</sup> cm <sup>-2</sup> )	Flux Density at 1 keV ( $10^{-15}$ ergs s <sup>-1</sup> cm <sup>-2</sup> keV <sup>-1</sup> )	$L_x^c$ ( $10^{44}$ ergs s <sup>-1</sup> )	$\chi^2_{\nu}/(\text{dof})$
1	$2.0^{+0.2}_{-0.2}$		$12.6^{+0.1}_{-0.1}$	5.9 (8.6)	4.1	0.42 (0.29)	1.5 (14)
2		$2.7^{+0.2}_{-0.2}$	$12.0^{+0.3}_{-0.3}$	5.6 (3.3)	3.8	0.29 (0.19)	1.3 (14)
3	$2.27^{+0.2}_{-0.2}$		9.0 (fixed)	7.8 (6.8)	5.1	0.63 (0.25)	1.9 (8)
4		$2.29^{+1.0}_{-0.5}$	9.0 (fixed)	7.3 (3.0)	4.7	0.34 (0.20)	2.0 (8)

<sup>a</sup> Fits 1 and 3 incorporate a power-law spectrum plus absorption due to cold material at solar abundances fixed to the Galactic value. Spectral fits 2 and 4 incorporate a Raymond-Smith thermal plasma model with the abundance set at 0.3 of the cosmic value. Fits 1 and 2 were performed in the observed energy range of 0.2–4 keV using LYNX. Fits 3 and 4 were performed in the observed energy range of 0.6–4 keV using XSPEC.

<sup>b</sup> Fluxes calculated in the ranges 0.2–2 keV and 2–10 keV (quoted in parentheses). X-ray fluxes are not corrected for Galactic absorption.

<sup>c</sup> Luminosities calculated in the ranges 0.2–2 keV and 2–10 keV (quoted in parentheses). Luminosities are in the rest frame and are corrected for Galactic absorption.



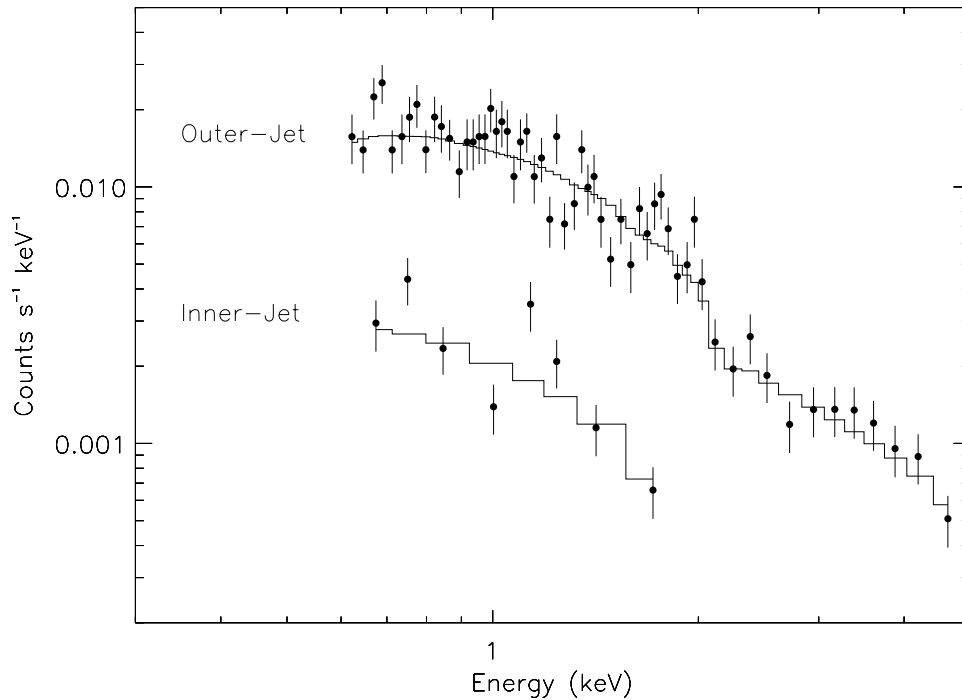


FIG. 7.—Spectra and best-fit models of the inner (fit 3 from Table 4) and outer (fit 3 from Table 5) jet components of PKS 0637–752

negligible for the outer jet component because of the extended nature of the emission combined with the relatively low count rate of  $0.025 \text{ counts s}^{-1}$ . We combined a subset of the observations of PKS 0637–752 listed in Table 1 to produce spectra of total exposure 32,931 s for node 0 of S3 and 70,700 s for node 1 of S3. The XSPEC and LYNX spectral fits were performed in the 0.6–6 keV range and 0.2–6 keV range, respectively. Plausible emission mechanisms for the production of the observed X-rays from the knots are synchrotron self-Compton and thermal bremsstrahlung emission from a compressed shocked medium. To distinguish between possible emission mechanisms, we fit the composite knot spectrum with absorbed power-law and thermal-plasma models. More complex models were not pursued because of the relatively low counts in the composite spectrum (see Table 1) and the present uncertainties in the low-energy instrumental response. Our results are pre-

sented in Table 5. Spectral fits with thermal and power-law models provide similar reduced  $\chi^2_{\nu}$ . The 2–10 keV luminosity of the outer jet region, assuming an absorbed power-law model (fit 1 in Table 5), is  $2.2 \times 10^{44} \text{ ergs s}^{-1}$ . No significant emission lines are detected in the outer jet spectrum. The composite spectrum for the outer jet of PKS 0637–752 with best-fit model (fit 3 in Table 5) is shown in Figure 7.

### 2.6. Properties of Sources in the Near Vicinity of PKS 0637–752

Several relatively X-ray bright sources (count rates above  $2 \times 10^{-3} \text{ counts s}^{-1}$ ) were detected on CCD S3 in the vicinity of PKS 0637–752. In Table 6 we list their coordinates, count rates, and distances from the core of PKS 0637–752. We searched the USNO catalog and found optical counterparts within  $1''$  in only five out of the 12 sources. No

TABLE 5

MODEL PARAMETERS DETERMINED FROM SPECTRAL FITS TO THE CHANDRA ACIS-S SPECTRA OF THE OUTER JET COMPONENT OF PKS 0637–752

Fit <sup>a</sup>	$\Gamma$	$T$ (keV)	$N_{\text{H}}$ ( $z=0$ ) ( $10^{20} \text{ cm}^{-2}$ )	Flux <sup>b</sup> ( $10^{-13} \text{ ergs s}^{-1} \text{ cm}^{-2}$ )	Flux Density at 1 keV ( $10^{-14} \text{ ergs s}^{-1} \text{ cm}^{-2} \text{ keV}^{-1}$ )	$L_{\text{X}}^{\text{c}}$ ( $10^{44} \text{ ergs s}^{-1}$ )	$\chi^2_{\nu}/(\text{dof})$
1.....	$1.83^{+0.1}_{-0.1}$		$11.8^{+0.3}_{-0.3}$	0.40 (0.75)	2.8	2.3 (2.3)	2.0 (49)
2.....		$3.8^{+0.2}_{-0.2}$	$11.8^{+0.1}_{-0.1}$	0.43 (0.41)	3.0	2.0 (1.9)	1.9 (49)
3.....	$1.85^{+0.08}_{-0.08}$		9.0 (fixed)	0.50 (0.82)	3.3	2.7 (2.5)	1.3 (85)
4.....		$5.6^{+1.1}_{-0.6}$	9.0 (fixed)	0.48 (0.61)	3.2	1.9 (2.4)	1.4 (85)

<sup>a</sup> Fits 1 and 3 incorporate a power-law spectrum plus absorption due to cold material at solar abundances fixed to the Galactic value. Fits 2 and 4 incorporate a Raymond-Smith thermal plasma model plus absorption due to cold material. Metal abundances were held fixed at 0.3 for fits 2 and 4. Spectral fits 3 and 4 were performed with XSPEC in the observed energy range of 0.6–7 keV with simultaneous fits to spectra extracted from nodes 0 and 1. Fits 1 and 2 were performed with LYNX in the observed energy range 0.2–7 keV with events extracted from node 1 only.

<sup>b</sup> Fluxes calculated in the ranges 0.2–2 keV and 2–10 keV (quoted in parentheses). X-ray fluxes are not corrected for Galactic absorption.

<sup>c</sup> Luminosities calculated in the ranges 0.2–2 keV and 2–10 keV (quoted in parentheses). Luminosities are in the rest frame and are corrected for Galactic absorption.

TABLE 6  
SOURCES IN THE NEAR VICINITY OF PKS 0637–752

Object	X (pixel)	Y (pixel)	R.A. (J2000)	Decl. (J2000)	Distance <sup>a</sup> (arcmin)	Count Rate (10 <sup>-2</sup> counts s <sup>-1</sup> )
CXO J063551.5–751528 .....	4149	4209	6 35 51.5	–75 15 28	0.89	0.71 ± 0.06
CXO J063538.3–751510 .....	3655	4007	6 35 38.3	–75 15 10	1.25	1.19 ± 0.08
CXO J063630.3–751522 .....	3705	3987	6 36 30.3	–75 15 22	2.98	0.37 ± 0.04
CXO J063607.2–751906 .....	3897	3257	6 36 07.2	–75 19 06	3.16	0.27 ± 0.04
CXO J063635.5–751659 .....	4667	4053	6 36 35.5	–75 16 59	3.25	0.56 ± 0.05
CXO J063551.2–751929 .....	4047	4173	6 35 51.2	–75 19 29	3.26	0.26 ± 0.04
CXO J063642.1–751649 .....	3019	4185	6 36 42.1	–75 16 49	3.63	1.24 ± 0.08
CXO J063446.7–751517 .....	4051	3683	6 34 46.7	–75 15 17	4.01	0.30 ± 0.04
CXO J063431.6–751627 .....	3925	3729	6 34 31.6	–75 16 27	4.85	0.64 ± 0.06
CXO J063500.3–752006 .....	3745	4185	6 35 00.3	–75 20 06	4.90	0.29 ± 0.04
CXO J063522.0–752107 .....	4275	3483	6 35 22.0	–75 21 07	5.17	0.36 ± 0.04
CXO J063438.0–751921 .....	4441	3605	6 34 38.0	–75 19 21	5.40	0.23 ± 0.03

NOTE.—Units of right ascension are hours, minutes, and seconds, and units of declination are degrees, arcminutes, and arcseconds.

<sup>a</sup> Distance from core of PKS 0637–752.

counterparts were found in the NED and SIMBAD catalogs.

### 3. DISCUSSION

In Figure 8, we present the SED of the WK7.8 knot of PKS 0637–752. The radio observations of PKS 0637–752 were performed at ATCA at 4.8 and 8.6 GHz. The 4.8 and 8.6 GHz beam width is  $\sim 2''$  and  $\sim 1''$  FWHM, respectively. The spectral indices and flux densities of the resolved components of the core, jet, and knots are presented in Table 7. Values for the optical flux density were obtained from the recent *Hubble Space Telescope* WFPC2 observations (Schwartz et al. 2000 and references therein).

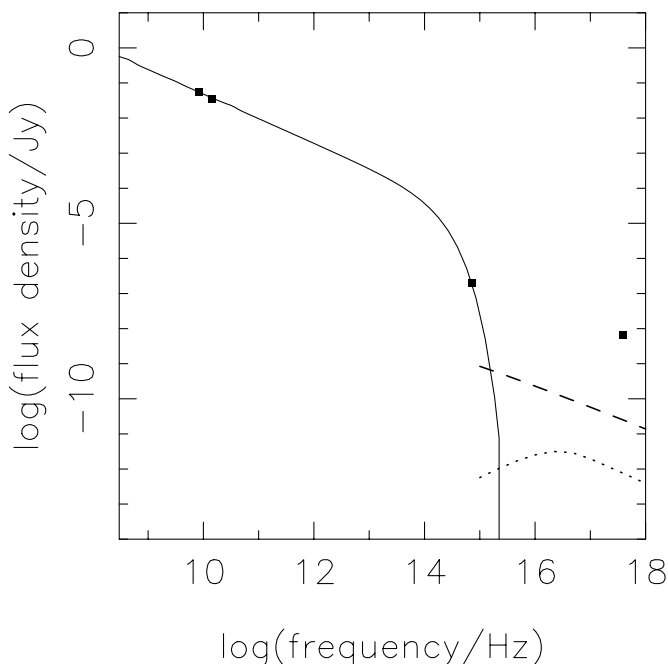


FIG. 8.—Spectral energy distribution for knot WK7.8 in the PKS 0637–752 jet. The solid line is the synchrotron component, the dashed line is the SSC component, and the dotted line is the Compton-scattered CMB component, as discussed in § 3 and Schwartz et al. (2000). The model components are based on equipartition assumptions.

The SED shows that a single-component power-law synchrotron model cannot explain the combined radio, optical, and X-ray flux densities since the optical lies far below a power-law interpolation between the radio and X-ray measurements. We also tested whether SSC emission or inverse Compton scattering of cosmic microwave background (CMB) photons could explain the observed X-ray emission. The model components in Figure 8 are for the case of equipartition between the magnetic field and electron energy densities and assume a sphere of radius  $0''.15$  and a power-law electron number spectrum of slope 2.4 between 100 MeV and 230 GeV, steepening by unity at 30 GeV due to energy losses. A detailed description of the SSC and inverse Compton calculations and the assumptions made for the model parameters are presented in a companion paper (Schwartz et al. 2000). We estimate an equipartition field,  $B_{\text{eq}}$ , of about  $2 \times 10^{-4}$  G. Based on this  $B_{\text{eq}}$ -value, both SSC and IC on the CMB underpredict the X-ray flux by several orders of magnitude. Thermal models were also considered. Assuming a plasma temperature of 10 keV, an emission volume of  $4 \times 10^{-3}$  arcsec<sup>3</sup> and a 2–10 keV luminosity of  $1 \times 10^{42}$  ergs s<sup>-1</sup>, we estimate a plasma density of about  $1 \text{ cm}^{-3}$ . The derived rotation measures (RMs) for radio waves propagating through such a dense plasma are quite large, inconsistent with the recent radio ATCA observations at 4.8 and 8.6 GHz (Schwartz et al. 2000; Lovell et al. 2000). These observations show  $\text{RM} \sim 80 \text{ rad m}^{-2}$  in the

TABLE 7  
RADIO SPECTRAL INDICES AND FLUX DENSITIES OF  
PKS 0637–752 COMPONENTS

Component	4.8 GHz Flux Density (Jy)	8.6 GHz Flux Density (Jy)	$\alpha_E$
Core .....	6.373	6.343	–0.01
Inner west jet .....	0.321	0.200	0.81
Outer west jet .....	0.167	0.095	0.97
East jet .....	0.206	0.110	1.08
Total cleaned flux .....	$7.03 \pm 0.02$	$6.72 \pm 0.02$	

NOTES.—All radio spectral energy indices follow the convention of flux density  $\propto \nu^{-\alpha_E}$ , where  $\alpha_E = (\Gamma - 1)$ . Note that the inner and outer west radio jets are defined as the components of the jet before and after the bend at WK9.7;  $1 \mu\text{Jy}$  is equivalent to  $10^{-29}$  ergs  $\text{cm}^{-2} \text{ s}^{-1} \text{ Hz}^{-1}$ .

core but no Faraday rotation in the jet, with an upper limit of  $\pm 10 \text{ rad m}^{-2}$ . A contrived geometry where the jet collides with a giant molecular cloud in a companion galaxy producing thermal X-rays, but from our line of sight the cloud is located behind the jet, may explain the nondetection of Faraday rotation in the jet.

An examination of the radio and X-ray brightnesses of different parts of the main emission region in the jet suggests that the X-ray brightness to radio brightness ratio is remarkably constant out to the last knot (WK9.7), where the X-rays are relatively fainter. The interpretation of the change of X-ray brightness between WK8.9 and WK9.7 depends, however, on the emission process: if the X-radiation has a synchrotron origin, then the emitting electrons must be locally accelerated, and the change in X-ray brightness of WK9.7 would be telling us about changes in particle acceleration at different points in the jet. If the X-rays have an inverse Compton origin, then it is possible that the brightness change is entirely due to aging of an electron population accelerated in WK8.9, but then other difficulties in understanding the energetics of the source must be faced (see Schwartz et al. 2000 for further discussion).

#### 4. CONCLUSIONS

*Chandra's* unique resolving-power capabilities open a new era in X-ray astronomy. We anticipate that many more radio jets and knots will be resolved in future observations with *Chandra*. The simultaneous spatial and spectral information provided with the *Chandra/ACIS* combination allows for accurate estimates of the size and spectral densities of the knots in extragalactic radio jets, which leads to tighter constraints on models that attempt to explain the X-ray emission. The standard emission processes usually invoked to explain X-ray emission from jets cannot explain the X-ray observations of PKS 0637–752. In particular, simple synchrotron models and equipartition SSC models underpredict the X-ray flux of the knots by many orders of magnitude. Thermal models predict shocked plasma densities and rotation measures that are too large. Particular contrived geometries of the jet and interacting molecular cloud may, however, explain the nondetection of Faraday rotation in the radio observations. More complex models that invoke inhomogeneities and/or nonequipartition and/or an extra photon source to explain the X-ray emission as inverse Compton are presented in Schwartz et al. (2000).

A careful spatial analysis combining most of the available observations of PKS 0637–752 has resolved the jet and at least four knots along the jet. The X-ray knots are 5"7, 7"8, 8"9, and 9"7 from the core of PKS 0637–752, in good agreement with the locations seen in the radio image. The X-ray knots are not individually resolved, and the upper limit on their diameter is  $\sim 0".4$ . The radio knots from the ATCA image are unresolved with an upper limit on their diameter also of  $\sim 0".4$ . However, our VLBI observations

(Schwartz et al. 2000; Lovell et al. 2000) have been re-analyzed to search for compact components close to the radio knots, and we find that the knots are indeed resolved at 0"05 resolution at 5 GHz, with less than 5 mJy remaining at this resolution. This suggests that they are low surface brightness “hot spots.”

The spectral analysis of the core, jet, and knot components has been quite complex due to the different non-optimal configurations used for each observation and the present uncertainty in several of the *Chandra/ACIS* calibration data sets. Having quoted the above caveat, we summarize the spectral analysis of the core and jet as follows:

1. The core flux and spectral shape are consistent with those measured with *ASCA*. However, we do not detect the emission line near 1 keV claimed in a recent *ASCA* observation of PKS 0637–752. The HPR for *ASCA* is about 3', so one possible explanation for this discrepancy is that the emission line claimed to be detected with *ASCA* may originate from a nearby unresolved source. We have detected three relatively weak X-ray sources within 3' of PKS 0637–752. However, the spectra of these sources do not show any prominent 1 keV emission lines that could explain the *ASCA* results.

2. The X-ray spectrum of the inner jet component appears to be slightly steeper than that of the outer jet region (see Tables 4 and 5). A difference in spectral slopes may be explained as follows: A population of synchrotron-emitting relativistic electrons in the inner jet region are undergoing radiation losses and producing the observed steeper spectra (X-ray and radio spectral indices  $\alpha_E \sim -1.0$ ). As these electrons enter the outer jet region (6"5–11"5 away from core), they are reaccelerated in a shock or some other structure to produce a flatter spectrum (X-ray and radio spectral indices  $\alpha_E \sim -0.8$ ). As they age past 11"5, the radio spectrum steepens again (radio spectral index  $\alpha_E \sim -1.0$ ). Also, in the region 11"5 away from the core where the highest energy electrons may plausibly have lost all their energy, the X-rays turn off as expected.

3. Spectral fits to the outer jet spectrum assuming thermal and power-law models yield similar  $\chi^2$  values. The outer jet region is relatively bright in X-rays with a 2–10 keV luminosity of  $2.2 \times 10^{44} \text{ ergs s}^{-1}$  (fit 1 in Table 5). The best-fit value of the X-ray luminosity of the outer jet is not sensitive to the assumed emission process. The good agreement in X-ray and radio spectral slopes in the inner and outer jet regions strongly suggests that there is substantial electron acceleration in the knot complexes WK7.8 and WK8.9.

We would like to thank Eric Feigelson for helpful comments, Martin Hardcastle for software used to generate Figure 8, and Kenneth Lanzetta for providing the optical flux density of knot WK7.8 used in Figure 8. This work was supported by NASA grant NAS 8-38252.

#### APPENDIX

##### LYNX: A SIMULATED-BASED SPECTRAL FITTING TOOL

Astrophysical X-ray spectra are commonly analyzed by creating parameterized models for the incident spectra, folding these models through the telescope and instrument responses, and then adjusting the parameters by minimizing a metric such

as  $\chi^2$  formed between the observed and modeled spectra. A tool that uses this approach and is widely used to fit astrophysical X-ray spectra observed from a variety of X-ray satellites is XSPEC. The telescope's effective area dependence with off-axis angle combined with the detector's quantum efficiency dependence with energy are usually incorporated into an auxiliary response file while the response of a detector to monoenergetic photons of energy  $E$  are incorporated into a spectral redistribution matrix. The spectral redistribution matrix is usually created from parameterizing the output of CCD simulations of input monoenergetic spectra. One approximation of forward fitting CCD spectra using telescope and detector response matrices is that the simulated CCD spectra are uniquely defined for a given model and set of input model parameters. In reality, however, several physical processes within CCDs are nondeterministic such as fluorescent yields, absorption depths, and photon escape probabilities, and detected spectra for identical incident spectra will in general be slightly different. This effect becomes more noticeable for spectra containing a low number of counts.

We have developed the tool LYNX that employs the forward fitting approach to infer incident astrophysical spectra. However, it differs from the conventional deterministic tools, such as XSPEC, in that the mirror and detector characteristics are determined by incorporating Monte Carlo simulators.

In particular, LYNX links to the ray-trace tool MARX (Wise et al. 1997) to simulate the mirror response and to the PSU ACIS simulator (Townsend et al. 2000, in preparation) to provide the CCD response. Astrophysical spectra obtained with ACIS are initially fit with the standard X-ray spectral fitting package XSPEC to provide an initial guess for LYNX. The modeled incident spectrum is propagated through the *Chandra* mirrors and ACIS components with the MARX and the PSU ACIS simulators, respectively. A merit function that incorporates the differences between the observed and simulated spectra spectrum is minimized using a downhill simplex method to yield the best-fit model parameters. LYNX simulates the propagation of individual photons through the HRMA/ACIS configuration and also takes into account the possible overlap of the resulting charge clouds within each exposure. The spectra produced through LYNX therefore will simulate pileup. The present version of LYNX also allows fitting spectra of any grade selection, corrects for vignetting, and accounts for the dither motion of the source across the CCD.

#### REFERENCES

- Arnaud, K. A. 1996, in ASP Conf. Ser. 101, *Astronomical Data Analysis Software and Systems V*, ed. G. H. Jacoby & J. Barnes (San Francisco: ASP), 17
- Biretta, J. A., Stern, C. P., & Harris, D. E. 1991, *AJ*, 101, 1632
- Dickey, J. M., & Lockman, F. J. 1990, *ARA&A*, 28, 215
- Elvis, M., & Fabbiano, G. 1984, *ApJ*, 280, 91
- Graessle, D. E., et al. 1993, *Proc. SPIE*, 1742, 203
- Harris, D. E., Carilli, C. L., & Perley, R. A. 1994, *Nature*, 367, 713
- Harris, D. E., et al. 2000, *ApJ*, 530, L81
- Harris, D. E., & Stern, C. P. 1987, *ApJ*, 313, 136
- Lawson, A. J., Turner, M. J. L., Williams, O. R., Stewart, G. C., & Saxton, R. D. 1992, *MNRAS*, 259, 743
- Lawson, A. J., & Turner, M. J. L. 1997, *MNRAS*, 288, 920
- Lovell, J. E. J., et al. 2000, in *Astrophysical Phenomena Revealed by Space VLBI*, ed. H. Hirabayashi, P. G. Edwards, & D. W. Murphy (Sagamihara: ISAS), 215
- Meisenheimer, K., Roser, H.-J., Hiltner, P. R., Yates, M. G., Longair, M. S., Chini, R., & Perley, R. A. 1989, *A&A*, 219, 63
- Schwartz, D. A., et al. 2000, *ApJ*, 540, L69
- van Speybroeck, L. P., Jerius, D., Edgar, R. J., Gaetz, T. J., Zhao, P., & Reid, P. B. 1997, *Proc. SPIE*, 3113, 89
- Weisskopf, M. C., & O'Dell, S. L. 1997, *Proc. SPIE*, 3113, 2
- Wise, M. W., Davis, J. E., Huenemoerder, Houck, J. C., Dewey, D., Flanagan, K. A., & Baluta, C. 1997, *The MARX 2.0 User Guide*, CXC Internal Document
- Yaqoob, T., George, I. M., Turner, T. J., Nandra, K., Ptak, A., & Serlemitsos, P. J. 1998, *ApJ*, 505, L87